materials

MDPI

Article

Mn-Doped Spinel for Removing Cr(VI) from Aqueous Solutions: Adsorption Characteristics and Mechanisms

Manman Lu [1], Zijian Su [2,*], Yuanbo Zhang [2,*], Hanquan Zhang [1], Jia Wang [2], Qian Li [2] and Tao Jiang [2]

[1] School of Resources and Safety Engineering, Wuhan Institute of Technology, Wuhan 430205, China
[2] School of Minerals Processing and Bioengineering, Central South University, Changsha 410083, China
* Correspondence: suzijian@csu.edu.cn (Z.S.); sintering@csu.edu.cn (Y.Z.)

Abstract: In this study, the manganese (Mn) was doped in the $MnFe_2O_4$ crystal by the solid-phase synthesis method. Under the optimum conditions (pH = 3), the max removal rate and adsorption quantity of Cr(VI) on $MnFe_2O_4$ adsorbent obtain under pH = 3 were 92.54% and 5.813 mg/g, respectively. The DFT calculation results indicated that the adsorption energy (E_{ads}) between $HCrO_4^-$ and $MnFe_2O_4$ is −215.2 KJ/mol. The Cr(VI) is mainly adsorbed on the Mn atoms via chemical bonds in the form of $HCrO_4^-$. The adsorption of Mn on the $MnFe_2O_4$ surface belonged to chemisorption and conformed to the Pseudo-second-order equation. The mechanism investigation indicated that the Mn in $MnFe_2O_4$ has an excellent enhancement effect on the Cr(VI) removal process. The roles of Mn in the Cr(VI) removal process included two parts, providing adsorbing sites and being reductant. Firstly, the Cr(VI) is adsorbed onto the $MnFe_2O_4$ via chemisorption. The Mn in $MnFe_2O_4$ can form ionic bonds with the O atoms of $HCrO_4^-/CrO_4^{2-}$, thus providing the firm adsorbing sites for the Cr(VI). Subsequently, the dissolved Mn(II) can reduce Cr(VI) to Cr(III). The disproportionation of oxidized Mn(III) produced Mn(II), causing Mn(II) to continue to participate in the Cr(VI) reduction. Finally, the reduced Cr(III) is deposited on the $MnFe_2O_4$ surface in the form of $Cr(OH)_3$ colloids, which can be separated by magnetic separation.

Keywords: chromium; reduction; adsorption; $MnFe_2O_4$; DFT calculation; spinel

Citation: Lu, M.; Su, Z.; Zhang, Y.; Zhang, H.; Wang, J.; Li, Q.; Jiang, T. Mn-Doped Spinel for Removing Cr(VI) from Aqueous Solutions: Adsorption Characteristics and Mechanisms. *Materials* **2023**, *16*, 1553. https://doi.org/10.3390/ma16041553

Academic Editor: Elza Bontempi

Received: 20 January 2023
Revised: 8 February 2023
Accepted: 10 February 2023
Published: 13 February 2023

1. Introduction

Chromium (Cr) widely exists in the surface and underground water as a common poisonous heavy metal. The Cr in water mainly comes from industrial discharges, such as leather tanning, electroplating, metal plating, and chemical manufacturing [1–3]. There are two primary species of Cr, trivalent (Cr (III)) and hexavalent (Cr (VI)) ions in the aqueous system [4], and the toxicity and mobility of Cr are highly dependent on its existing species [5]. It is widely believed that the toxicity of Cr (VI) is much higher than that of Cr (III), and Cr(VI) is highly carcinogenic and teratogenic [6]. The hypertoxic Cr(VI) in the natural environment could cause a range of diseases and pose a major threat to humans and ecology [7,8]. Therefore, many present researchers have focused on the field of Cr(VI) reduction [9,10]. Among this research, the adsorption-reduction method for Cr(VI) removal has received the most extensive research [11]. Furthermore, some biosorbents have been developed for heavy-metal removal [12].

The current Cr(VI) reduction methods primarily include chemical, electrochemical, photocatalytic, and biological reduction processes [13–16]. Most of the literature has shown that adsorption is a prerequisite for Cr(VI) reduction [17]. Many adsorbents have been prepared to achieve the adsorption-reduction reaction of Cr(VI) on their surfaces [18–20]. Among these adsorbents, metallic oxide, especially spinel-type materials, has been most extensively investigated due to its good magnetic properties, easy synthesis, low cost, and chemical stability. Many published literature studies have verified that Cr(VI) can be reduced by certain low-valence metal ions such as Fe(II) and Mn(II) in spinel materials [21,22].

Mu et al. [23] verified that Mn(II) could promote the Cr(VI) reduction via oxalic acid. In the Cr(VI) reduction process, Cr(VI) oxidized Mn(II) to Mn(III). Then, the oxidized Mn(III) acted as an electron bridge, transferring the electron from oxalic acid to Cr(VI). Another recent paper adopted a synthetic Mn_3O_4@ZnO/Mn_3O_4 composite to reduce Cr(VI) [24]. As an electron carrier, Mn acted in the role of a catalyst during the Cr(VI) reduction. Another research study elaborated on the adsorption mechanisms of Cr(VI) on the surface of manganese oxide in detail [25]. The researchers found that Cr(VI) adsorption belongs to more than one type of reaction. The Cr(VI) can bind to functional groups by the inner-and outer-sphere chromate complexes under different pH values.

Based on the previous research on the effects of Mn on the Cr(VI) reduction, we synthesized a novel Mn-doped spinel to remove the Cr(VI) from the Cr-bearing solution. The appropriate amount of natural ferromanganese and hematite ore powder was mixed and subsequently roasted under suitable conditions, and Mn replaced the Fe atom at the A site in the Fe_3O_4 spinel, forming $MnFe_2O_4$ [26]. Some reports have manifested that the $MnFe_2O_4$ has good adsorbing ability on Cr(VI) [27–32]. However, these researchers primarily focused on the adsorption characteristics of Cr(VI) on $MnFe_2O_4$, and the mechanism of Cr(VI) removal had been neglected. In this research, DFT calculation was introduced to reveal the adsorption mechanism of Cr(VI)on the $MnFe_2O_4$ surface. A molecular model was built to study the interaction type between Cr(VI) and the $MnFe_2O_4$ surface. What is more, the $MnFe_2O_4$ material used in the previous research is synthesized from pure chemical raw materials, and its crystallinity, morphology, and impurity content are different from the $MnFe_2O_4$ prepared from natural minerals. Indeed, the $MnFe_2O_4$ is more special as an adsorbent compared with other kinds of spinel because of the non-negligible role of Mn in the Cr(VI) removal process. Some investigations have already manifested that Mn ions in $MnFe_2O_4$ have higher reaction activity compared to the Fe ions in Fe_3O_4 [33,34].

The critical point of this study is to deeply analyze the roles of Mn in the Cr(VI) removal process on the $MnFe_2O_4$ surface by means of the XPS test and DFT calculation. Furthermore, the adsorption characteristics of Cr(VI) adsorption on the $MnFe_2O_4$ adsorbent were investigated by the batch adsorption experiments. This study attempts to explain the adsorption mechanisms of the Cr(VI) adsorption on the $MnFe_2O_4$ adsorbent.

2. Materials and Methods

2.1. Materials

In the previous work, our group invented a novel high-temperature solid-phase synthesis method to prepare the $MnFe_2O_4$ adsorbent [26]. To begin with, the ferromanganese ore and hematite ore powders were evenly mixed, and the stoichiometric ratio of Mn and Fe in mixed raw materials was 1:2. The roasting temperature and time were controlled at 1200 °C and 1 h. The mixture briquettes were broken and ground to −0.074 mm, accounting for 70 wt% after roasting. Then the $MnFe_2O_4$ particles and the gangue minerals were separated by magnetic separation. The obtained $MnFe_2O_4$ particles continued to be nano-ground to the size of 200 nm (d0.5 = 200 nm). The nano-$MnFe_2O_4$ particles were used as a magnetic adsorbent for the Cr(VI) removal.

All chemicals used in this research were of analytical grade. The simulated Cr(VI)-bearing solution was prepared using $K_2Cr_2O_7$ (Sinopharm Group Co., Ltd., Beijing, China). The pH was adjusted with 0.1 M HCl and 0.1 M NaOH solutions.

2.2. Adsorption Characteristics

Adsorption experiments were conducted under isothermal conditions using the batch method. The isothermal adsorption experiments were conducted to investigate the Cr(VI) adsorption characteristics of the $MnFe_2O_4$ adsorbent. A certain weight of the $MnFe_2O_4$ adsorbent was added to an Erlenmeyer flask with a 50 mL Cr(VI) solution to conduct the adsorption experiments. The mixed solutions were oscillated for 24 h to ensure the Cr(VI) achieved equilibrium. Then the filtrates were obtained by filtering through a 0.45 μm membrane filter. The equilibrium concentration of Cr(VI) was measured by ICP-

MS analysis. The adsorbing amount of Cr(VI) on the $MnFe_2O_4$ adsorbent under various experimental conditions was calculated according to the following equation:

$$q_e = \frac{(C_o - C_e) \cdot V}{m} \quad (1)$$

where q_e is the adsorbing amount of Cr(VI) on the $MnFe_2O_4$ adsorbent ($mg \cdot g^{-1}$); C_o and C_e are the initial and equilibrium concentrations of the Cr(VI) solution ($mg \cdot L^{-1}$), respectively; V is the volume of the Cr(VI)-bearing solution; and m is the mass of the $MnFe_2O_4$ adsorbent.

The pH effect tests were conducted within the pH range of 1–10. The pH of the solution was adjusted by 0.1 M HCl and 0.1 M NaOH. The initial Cr(VI) concentration and $MnFe_2O_4$ dosage were controlled at 10 mg/L and 3 g/L, respectively. The adsorption kinetics of Cr(VI) on the $MnFe_2O_4$ were investigated by changing the oscillation time of the Cr(VI) adsorption. The oscillation times were changed from 5 to 720 min in this research, and the initial Cr(VI) concentration was controlled at 10 mg/L. The Cr(VI) adsorption data at the various oscillation time were analyzed according to the following two models, the pseudo-first-order equation and the pseudo-second-order equation. The linear forms of these two models are listed below [30]:

$$\ln(q_e - q_t) = \ln q_e - k_1 t \quad (2)$$

$$\frac{t}{q_t} = \frac{1}{k_2 {q_e}^2} + \left(\frac{1}{q_e}\right) t \quad (3)$$

where q_e and q_t are the adsorption amounts of Cr(VI) at equilibrium and a certain time t ($mg \cdot g^{-1}$), respectively; k_1 and k_2 are the rate constants of the pseudo-first-order equation and the pseudo-second-order equation, respectively.

The isothermal adsorption experiments were conducted with the initial Cr(VI) concentration range of 1–100 mg/L. The obtained equilibrium concentrations were fitted via the Langmuir and Freundlich models. The linearized Langmuir and Freundlich isotherm models are expressed as the following equations [31]:

$$C_e/q_e = C_e/q_m + 1/(k_L q_m) \quad (4)$$

$$log q_e = log k_F + (1/n) log C_e \quad (5)$$

where q_e ($mg \cdot g^{-1}$) is the amount of Cr(VI) adsorbed per weight unit of the $MnFe_2O_4$ adsorbent after equilibrium; C_e ($mg \cdot L^{-1}$) is the equilibrium concentration of Cr(VI) in the solution; q_m ($mg \cdot g^{-1}$) is the maximum adsorption capacity of the adsorption; K_L is a constant related to the heat of adsorption ($L \cdot mg^{-1}$); K_F ($mg^{1-n} \cdot L^n \cdot g^{-1}$) is a constant related to the extent of adsorption; and 1/n is related to the intensity of adsorption.

2.3. Characterization

The X-ray powder diffraction (XRD) patterns of the synthetic $MnFe_2O_4$ before and after nano-scale grinding were detected by a diffractometer with Cu Kα radiation (RIGAKU D/Max 2500, Tokyo, Japan). The tube current and voltage were 250 mA and 40 kV, the scanning range was 10–70°, and the step size was 0.02°. A vibrating sample magnetometer was adopted to measure the magnetism properties of the $MnFe_2O_4$ adsorbent (PPMS Dynacool, Quantum Design, San Diego, CA, USA). The element composition and binding energies of atomic orbital on the $MnFe_2O_4$ surface before and after adsorbing Cr(VI) were investigated by the XPS test (XPS, Mono 650 μm, 200 W, Al Kα, pass energy 20 eV). The scanning step size was 1.0 eV for the full scan and 0.1 eV for the narrow scan. Zeta potential measurements were conducted using a zetasizer under a wide pH range from 3 to 10 at 25 °C, and the pH value was adjusted using 0.1 M HCl and NaOH. The particle size distribution was characterized by a laser particle analyzer (Malvern Mastersizer 2000, Malvern, UK). The specific surface area and pore volume of the $MnFe_2O_4$ adsorbent were measured by nitrogen adsorption-desorption on a specific surface area with a pore analyzer.

The slab supercell that consists of a (2 × 2) unit cell of $MnFe_2O_4$ (100) was constructed as the substrate. A vacuum of 20 Å was added to eliminate the interaction between two periodic slabs and H atoms were attached to O on the surface in acidic conditions ($MnFe_2O_4$-H (100)). The calculations were conducted under density functional theory, and the Vienna ab initio simulation (VASP) code 1, 2 was used to implement. The initial adsorption site was predicted by the simulated annealing method for locating a good approximation to the global minimum. Projector Augmented Wave (PAW) pseudopotentials are used with a cutoff energy of 400 eV for plane wave expansions. The GGA-PBE5 was used as an exchange-correlation function. The atomic relaxation was performed with a k-mesh of 1 × 1 × 1 until the force on each atom is less than 0.02 eV/Å. Moreover, van der Waals forces between the adsorbate and substrate were also corrected by the DFT-D26 dispersion corrections. After relaxation, a gamma-center k-mesh 2 × 2 × 1 was adopted for the ground state total energy calculation. The adsorption energy (Eads) was evaluated by:

$$\text{Eads} = \text{E(total)} - \text{E(sub)} - \text{E(ads)} \quad (6)$$

where E(total), E(sub), and E(ads) are the total energy of the $MnFe_2O_4$-H (100)-adsorbate complex, $MnFe_2O_4$-H (100), and adsorbates ($HCrO_4^-$, CrO_4^{2-} and $Cr_2O_7^{2-}$) in the same cell, respectively. According to this definition, a negative value is energetically favorable.

The transfer charge (Δchg) is the net charge on adsorbates:

$$\Delta\text{chg} = \sum_{i=1}^{n} A_i - A_i^0 \quad (7)$$

where A_i and A_i^0 are the self-consistent charge and the atomic charge of atom i, respectively. n is the total number of studied adsorbates. The negative value represents electron dissipation to the substrate and positive Δchg represents electron accumulation on the adsorbate.

3. Results

3.1. Characterization of $MnFe_2O_4$ Adsorbent

The effects of nano-scale grinding on the crystallinity and crystal integrity of $MnFe_2O_4$ were investigated by X-ray diffraction patterns. Figure 1a shows that the diffraction peaks at 29.95°, 35.33°, 56.42°, and 61.94° were considered to belong to the 220, 311, 511, and 440 crystal faces of $MnFe_2O_4$ [35], respectively. After grinding, the crystallinity of $MnFe_2O_4$ worsened and certain diffraction peaks disappeared. This result indicated that the strong mechanical grinding would damage the $MnFe_2O_4$ crystal to some extent. The magnetization shown in Figure 1d exhibited that the magnetization intensity of $MnFe_2O_4$ decreased sharply from 63.38 to 23.80 emu/g after grinding. The main reason is that the magnetism of $MnFe_2O_4$ is the macroscopic manifestation of the magnetic properties of many tiny magnetic domains inside it, and as the particle size decreases, the number of internal magnetic domains decreases, resulting in a weakening in the magnetism of nano-size $MnFe_2O_4$ particles. Fortunately, the magnetic saturation curves displayed in Figure 1d manifested that the saturation magnetic of nano-$MnFe_2O_4$ still retained 20 emu/g, illustrating that the $MnFe_2O_4$ adsorbent still had good magnetism and could be recovered by magnetic separation. The BET test manifested that the specific surface area of the $MnFe_2O_4$ adsorbent could achieve 31.997 m^2/g after nano-scale grinding. The zeta potential results exhibited in Figure 1c illustrated that the pHpzc (zero-point charge pH value) of the $MnFe_2O_4$ is 7.5. The $MnFe_2O_4$ adsorbent was positively charged within the pH range of 3–7.5. Therefore, there is an electrostatic attraction between electropositive $MnFe_2O_4$ particles and chromate ($HCrO_4^-$, CrO_4^{2-}, and $Cr_2O_7^{2-}$).

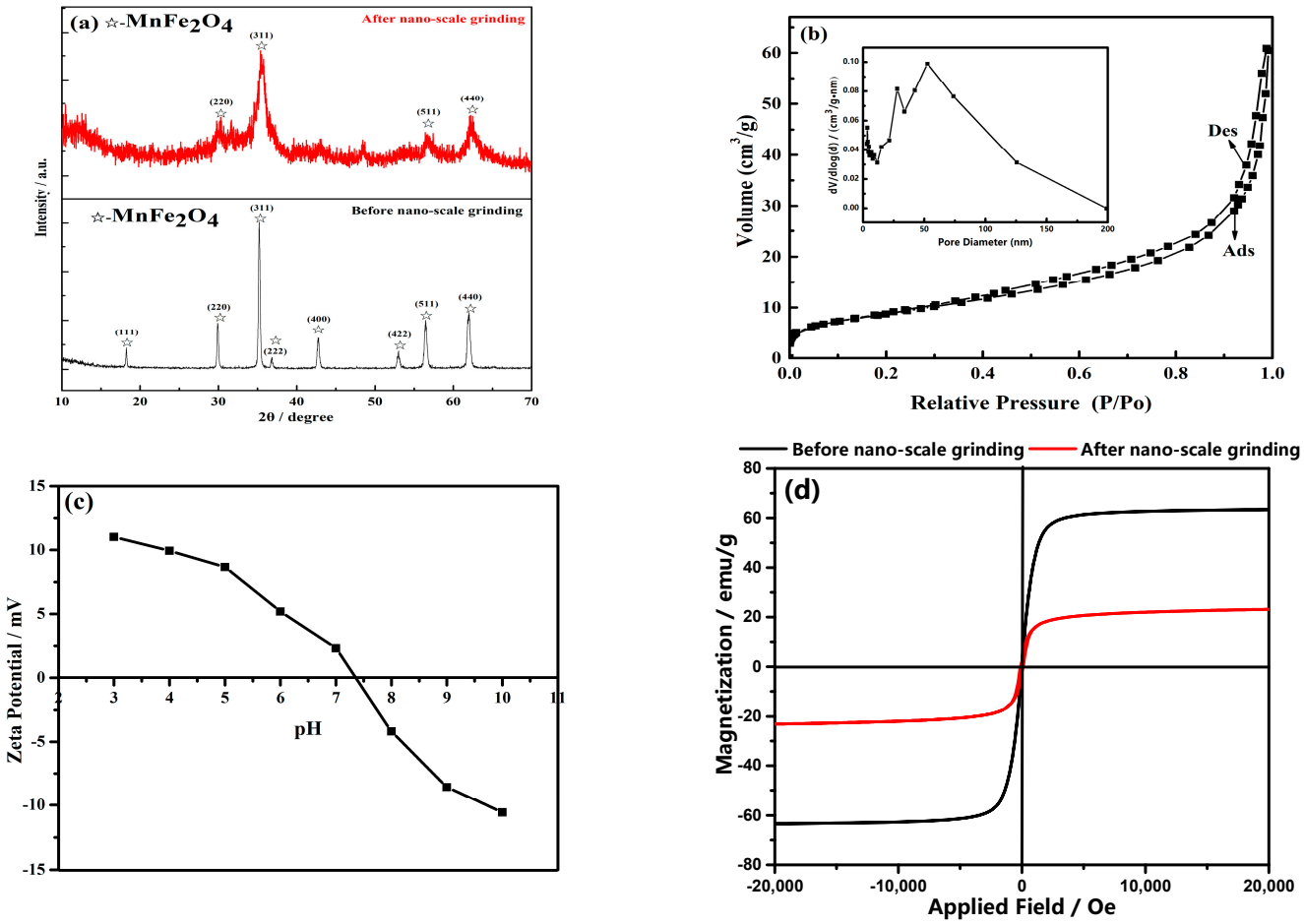

Figure 1. The XRD pattern of $MnFe_2O_4$ before and after nano-scale grinding (**a**); the BET adsorption−desorption curve of $MnFe_2O_4$ adsorbent (**b**); zeta potential of $MnFe_2O_4$ adsorbent (**c**); the magnetization hysteresis loops of $MnFe_2O_4$ before and after nano−scale grinding (**d**).

3.2. Adsorption Characteristics

3.2.1. Effect of the Initial pH

In this study, the Cr(VI) adsorption tests were conducted under pH values of 1 to 10. As shown in Figure 2a, the Cr(VI) removal first increased within the pH range of 1–3 and then continued to decline with an increasing pH. The Cr(VI) reduction in the acidic system conformed to the following equations [36,37]:

$$HCrO_4^- + 3e^- + 7H^+ \rightarrow Cr^{3+} + 4H_2O \quad (8)$$

$$Cr_2O_7^{2-} + 6e^- + 14H^+ \rightarrow 2Cr^{3+} + 7H_2O \quad (9)$$

The hydrogen ions participated in the Cr(VI) reduction, and this indicated that the acidic system is favorable for Cr(VI) reduction. Furthermore, according to the zeta potential tests of $MnFe_2O_4$, the electrostatic attraction between the $MnFe_2O_4$ and chromate is more reliable in a low-pH environment. However, when in a very strong acidic system (pH = 1 and 2), the reduction product Cr(III) could not be deposited on the $MnFe_2O_4$ surface by forming the $Cr(OH)_x$ compound due to the neutralization. This is the main reason that the Cr(VI) removal under pH = 1 and 2 is lower than that under pH = 3.

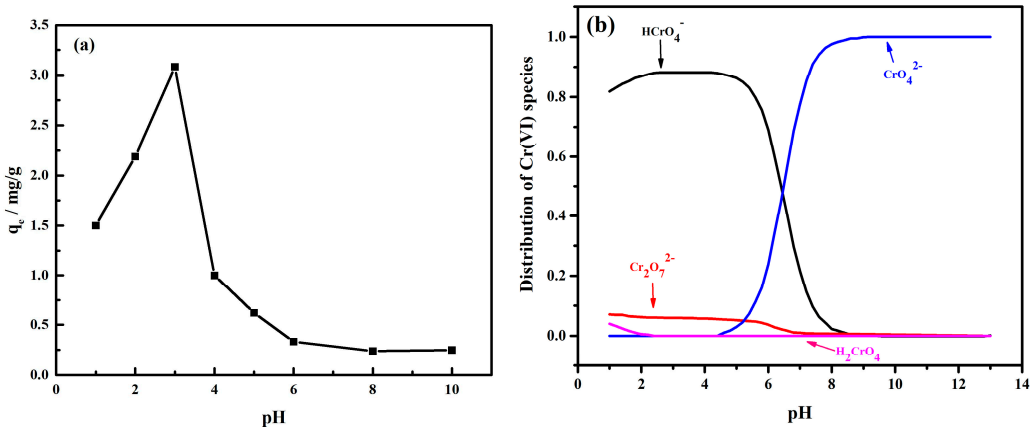

Figure 2. The Cr(VI) removal (**a**) and species (**b**) at various pH values.

3.2.2. Adsorption Kinetics

The time needed to reach the adsorption equilibrium was a significant value that decided the Cr(VI) removal efficiency. In this experiment, the Cr(VI) adsorption kinetics was determined by measuring the adsorption amount of Cr(VI) at various times. The adsorption kinetic curve of Cr(VI) is displayed in Figure 3a, and the fitting curves of the pseudo-first-order and pseudo-second-order equations are displayed in Figure 3b,c, respectively. The fitting parameters of the pseudo-first-order equation and pseudo-second-order models are given in Table 1.

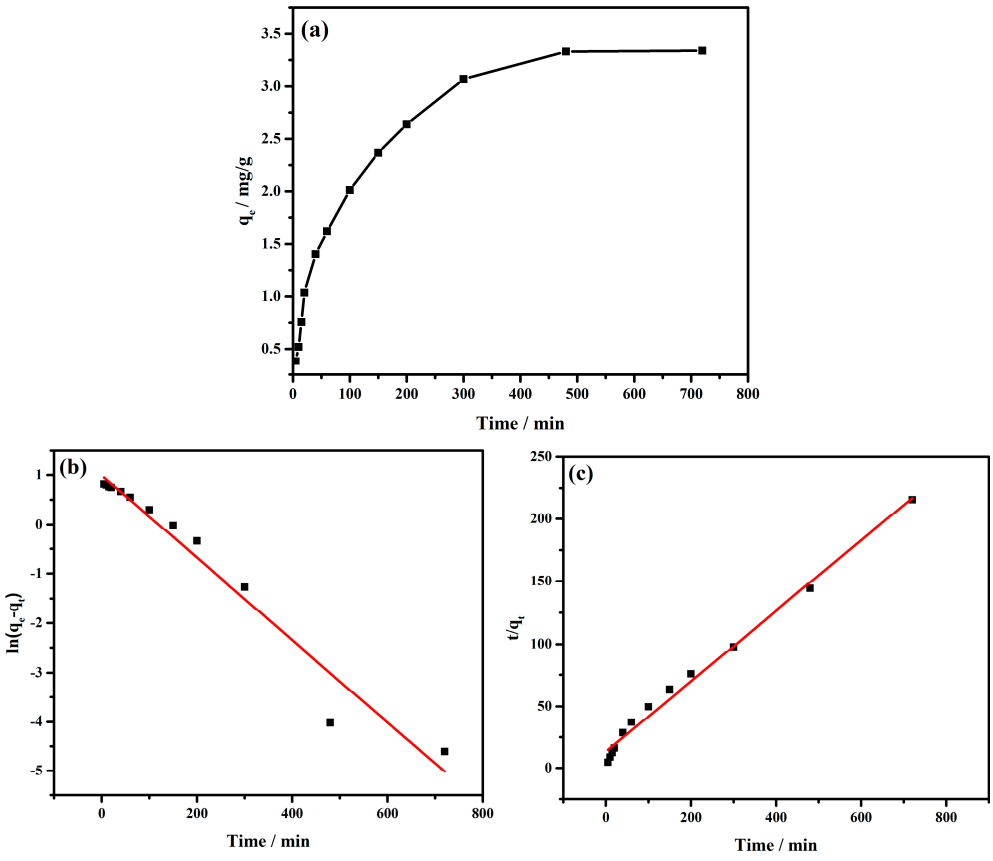

Figure 3. Adsorption kinetics analysis of Cr(VI) on $MnFe_2O_4$ adsorbent: (**a**) Adsorption amount of Cr(VI) at various times; (**b**) fitting line of the pseudo−first−order equation; (**c**) fitting line of the pseudo-second-order equation.

Table 1. Kinetic fitting parameters for the pseudo-first-order and pseudo-second-order equations for Cr(VI) adsorption onto the $MnFe_2O_4$ adsorbent.

		Pseudo-First-Order Equation			Pseudo-Second-Order Equation		
Adsorbate	**qe (mg/g)**	**qe,c (mg/g)**	**k1 (min^{-1})**	**R^2**	**qe,c (mg/g)**	**K2 ($g/mg \cdot min^{-1}$)**	**R^2**
Cr(VI)	3335	2698	0.00834	0.959	3538	0.00597	0.989

The adsorption kinetic curve of Cr(VI) is displayed in Figure 3a, and the fitting curves of the pseudo-first-order and pseudo-second-order equations are displayed in Figure 3b,c, respectively. The fitting parameters of the pseudo-first-order equation and pseudo-second-order models are given in Table 1. The correlation coefficient (R^2) of these two models indicated that the pseudo-second-order model was more suitable to describe the Cr(VI) adsorption kinetics on $MnFe_2O_4$ adsorbent. The result showed that the Cr(VI) adsorption achieved equilibrium in 480 min, and further extending the adsorption time could hardly affect the adsorption amount of Cr(VI). The above results manifested that Cr(VI) adsorption on the $MnFe_2O_4$ adsorbent belonged to chemisorption [38].

3.2.3. Adsorption Isotherm

As many papers reported, the adsorption isotherm model fitting was a common tool to understand the adsorption type between the adsorbent and adsorbate [39]. The Langmuir and Freundlich isotherm models fitting lines and parameters of Cr(VI) adsorption on the $MnFe_2O_4$ surface are shown in Figure 4 and Table 2, respectively.

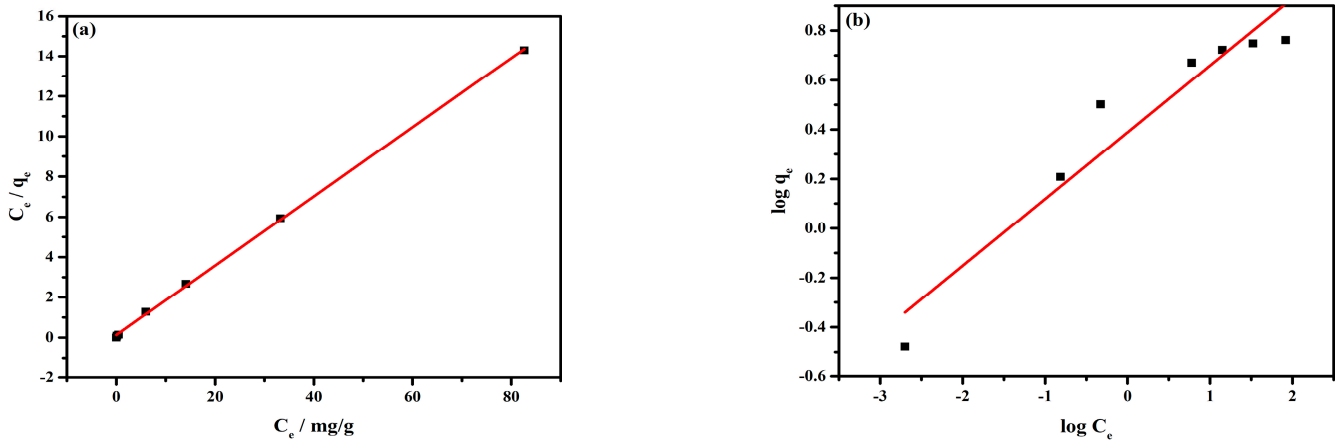

Figure 4. Langmuir (**a**) and Freundlich (**b**) isotherms for the adsorption of Cr(VI) onto the $MnFe_2O_4$ adsorbent.

Table 2. The parameters for Langmuir and Freundlich models for Cr(VI) adsorption onto the $MnFe_2O_4$ adsorbent.

T (K)	**Langmuir**			**Freundlich**		
	qm (mg/g)	**kL ($L \cdot mg^{-1}$)**	**R^2**	**kF ($mg^{1-n} \cdot Ln \cdot g^{-1}$)**	**1/n**	**R^2**
298	5813	1282	0.9995	2448	0.270	0.9121

The results illustrated that the max adsorption quantity of Cr(VI) is 5.813 mg/g. The correlation coefficient (R^2) of the Langmuir model is higher than that of the Freundlich model, showing that the Cr(VI) adsorption on the $MnFe_2O_4$ surface conformed to the Langmuir model. It was likely that the Cr(VI) adsorption tended to be monolayer adsorption [40]. Compared with other adsorbents, the adsorption capacity of the adsorbent in this study is lower. The main reason is that there are some impurities when using natural

minerals for synthesis. What is more, the solid-phase synthetic $MnFe_2O_4$ particles are coarse, while after grinding, their specific surface area is still much smaller than that of the liquid-phase synthetic $MnFe_2O_4$ particles.

3.3. Enhancement Mechanism of Mn on Cr(VI) Adsorption and Reduction

3.3.1. Cr(VI) Adsorption Analyses

The Cr(VI) removal process on the $MnFe_2O_4$ surface primarily included the adsorption and reduction process. The Cr(VI) could only be reduced after being adsorbed on the $MnFe_2O_4$ surface. As much of the literature has reported, the DFT calculation is a powerful tool to investigate the interaction reaction between two kinds of molecules [41,42]. In this study, the $MnFe_2O_4$ (100) surface, a typical low-index surface, was used to investigate the role of Mn in the Cr(VI) adsorption process.

Figure 5a shows the optimum structure of spinel-type $MnFe_2O_4$, the bond distances of Fe-Fe, Fe-Mn, Fe-O, and Mn-O are 3.011 Å, 3.530 Å, 4.760 Å, and 3.687 Å, respectively. However, according to the stern double-layer theory [43], when $MnFe_2O_4$ is placed in an aqueous solution, a layer of hydrogen or hydroxyl groups adsorbed on the surface of $MnFe_2O_4$ molecules exists, which is called the "positioning ion" [44]. In this study, the Cr(VI) adsorption process primarily occurred in the acidic solution, and the $MnFe_2O_4$-H molecule was dominant compared with $MnFe_2O_4$-OH. We built up a new structure of $MnFe_2O_4$-H by causing the hydrogen ion to adsorb on the surface of the $MnFe_2O_4$ molecule. The optimum structure of $MnFe_2O_4$-H is displayed in Figure 5b. The bond distances of Fe-H, Mn-H, and O-H were 1.500 Å, 1.610 Å, and 1.100 Å, respectively.

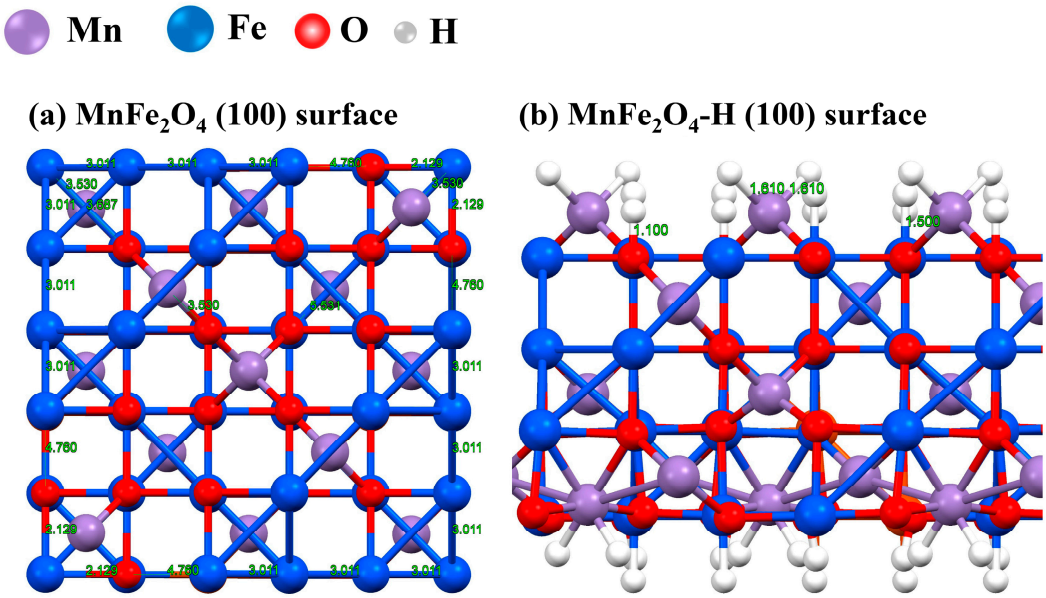

Figure 5. The optimum structure of (**a**) $MnFe_2O_4$ (100) surface and (**b**) $MnFe_2O_4$−H (100) surface.

Next, the groups of $HcrO_4^-$, CrO_4^{2-}, and $Cr_2O_7^{2-}$ were selected to conduct DFT calculations. The optimum structures of $MnFe_2O_4$−H−$HcrO_4^-$, $MnFe_2O_4$−H−CrO_4^{2-}, and $MnFe_2O_4$−H−$Cr_2O_7^{2-}$ are shown in Figure 6. Moreover, the adsorption energies and the bond distances of $HcrO_4^-$, CrO_4^{2-}, and $Cr_2O_7^{2-}$ on $MnFe_2O_4$-H (100) are listed in Table 3.

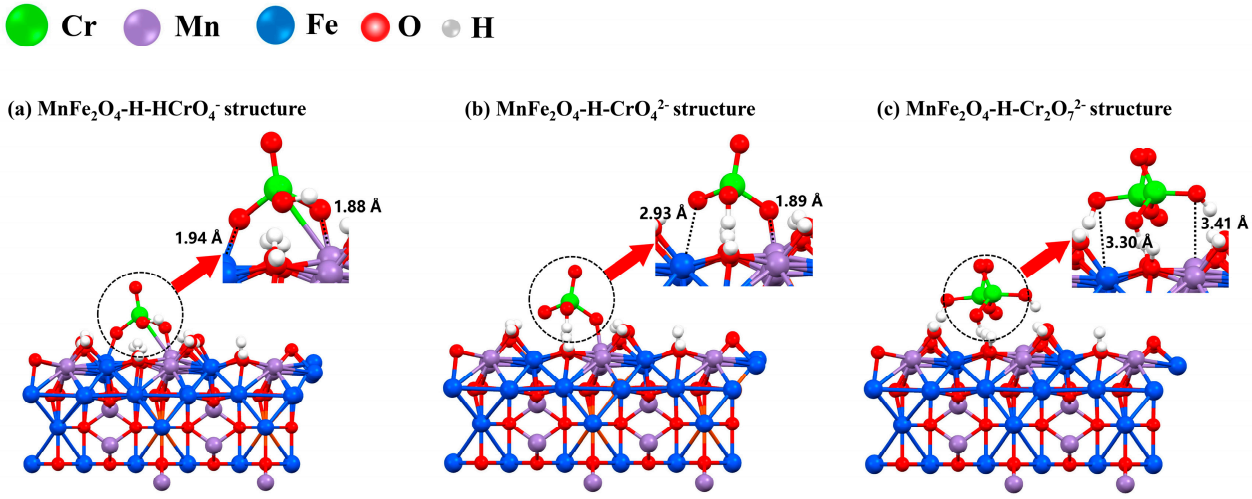

Figure 6. The optimum structure of $MnFe_2O_4-H-HcrO_4^-$ (**a**), $MnFe_2O_4-H-CrO_4^{2-}$, (**b**) and $MnFe_2O_4-H-Cr_2O_7^{2-}$ (**c**).

Table 3. Comparison of the results of this research with other related research.

Adsorbents	Metal Ions	Synthetic Raw Materials	Adsorption Capacity/mg/g	Refs
$MnFe_2O_4$	Cr(VI)	Natural minerals	5813	This study
BCMFC	Cr(VI)	Chemical reagents	178.6	[27]
Nano-$MnFe_2O_4$	Cr(VI)	Chemical reagents	31.5	[25]
$MnFe_2O_4/FeS_{X-0.5}$	Cr(VI)	Chemical reagents	43.36	[29]
MFO/C NPs	Cr(VI)	Chemical reagents	73.26	[30]

As shown in Table 4, the adsorption energies of $HcrO_4^-$, CrO_4^{2-}, and $Cr_2O_7^{2-}$ on the $MnFe_2O_4$-H surface were −215.2, −200.7, and −116.7 kJ/mol, respectively. The adsorption energy is an indicator of system stability calculated by subtracting the system's energy before and after adsorption [45]. In general, the higher the adsorption energy is, the more stable the system after adsorption is [46]. Therefore, it can be easily observed that $HcrO_4^-$ was the most easily adsorbed on the $MnFe_2O_4$ adsorbent. Moreover, it can also be observed that from the bond distances displayed in Table 3, in the $MnFe_2O_4-H-HcrO_4^-$ system, the O atom of $HcrO_4^-$ formed a chemical bond with the Mn atoms of $MnFe_2O_4$, providing high adsorption energy. As we know, the adsorption process is an essential link to the subsequent reduction [47,48]. The DFT calculation indicated that the $HcrO_4^-$ could be efficiently adsorbed by the Mn atoms of the $MnFe_2O_4$ via the chemical bonds. This efficient adsorption of Cr(VI) created a favorable environment for the subsequent Cr(VI) reduction by the Mn(II).

Table 4. The adsorption energy, the shortest distance between Mn/Fe and O, and the charge transfer between $MnFe_2O_4-H$ (100) and adsorbates.

	Eads/kJ/mol	D(Mn-O)/Å	D(Fe-O)/Å	Δchg
$HcrO_4^-$	−215.2	1.88	1.94	0.609
CrO_4^{2-}	−200.7	1.89	2.93	0.524
$Cr_2O_7^{2-}$	−116.7	3.41	3.30	0.032

Subsequently, the charge density distribution was calculated by VASP software to clarify the chemical bond type between the chromate and the $MnFe_2O_4$-H.

In general, the charges would be distributed at both ends of the bond in the electrostatic interaction or ionic bond [49]. In contrast, for the covalent bond, the charge would be distributed in the middle of the bond [50]. The charge density distribution shown in Figure 7 indicates that the charges of the Mn/Fe-O bonds in the $MnFe_2O_4$−H− $HcrO_4^-$ system were distributed at the ends of the bonds. This implied that the Mn/Fe-O bond belonged to the ionic bond. Similarly, CrO_4^{2-} was also adsorbed on the Mn atom of the $MnFe_2O_4$ adsorbent via the ionic bond, while during the $Cr_2O_7^{2-}$ adsorption process, the bonding had little effect on the charge distribution of the two molecules. Therefore, it could be suggested that the adsorption of $Cr_2O_7^{2-}$ on the $MnFe_2O_4$ surface is a type of physical adsorption via electrostatic attraction.

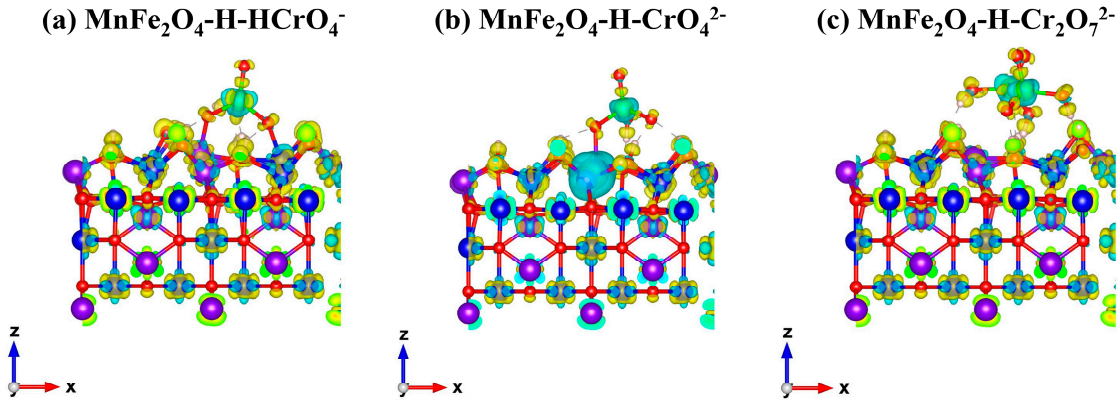

Figure 7. The charge density of $MnFe_2O_4$−H−$HcrO_4^-$ (**a**), $MnFe_2O_4$−H−CrO_4^{2-}, (**b**) and $MnFe_2O_4$−H−$Cr_2O_7^{2-}$ (**c**).

3.3.2. Cr(VI) Reduction Analyses

The chemical states on the $MnFe_2O_4$ surface before and after the Cr(VI) adsorption were investigated by the XPS test to explain the reduction mechanisms of Cr(VI). The XPS full-scanning spectra of the original $MnFe_2O_4$ adsorbent and $MnFe_2O_4$ adsorbed Cr(VI) under pH = 3 and 7 are shown in Figure 8. The main atom contents on the $MnFe_2O_4$ adsorbent surface before and after adsorbing Cr(VI) are displayed in Table 5.

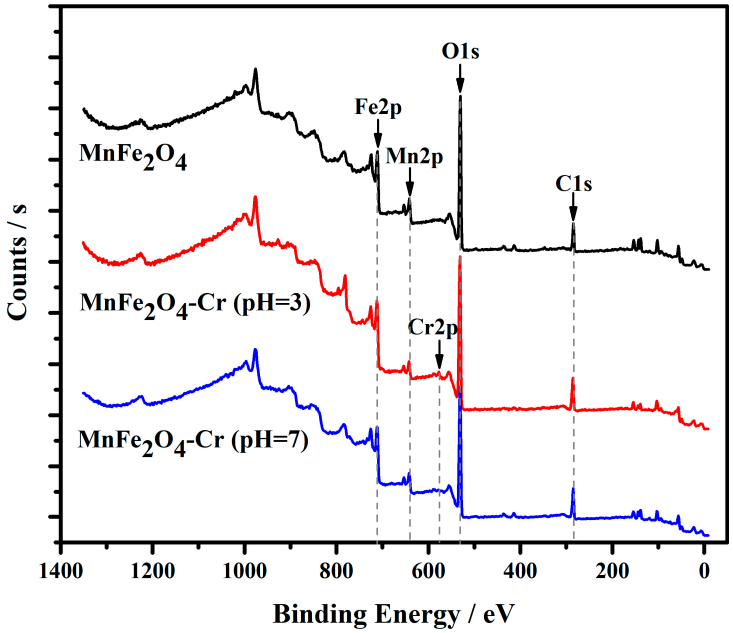

Figure 8. The XPS spectra of $MnFe_2O_4$ adsorbent, $MnFe_2O_4$−Cr (pH = 3), $MnFe_2O_4$-Cr (pH = 7).

Table 5. Atom contents of the surfaces of the three samples.

Elements	Atom Content of $MnFe_2O_4$/%	Atom Content of $MnFe_2O_4$-Cr (pH3)/%	Atom Content of $MnFe_2O_4$-Cr (pH7)/%
C1s	24.08	30.02	29.76
O1s	60.65	56.00	55.58
Fe2p	11.73	11.17	11.35
Mn2p	3.55	2.03	3.11
Cr2p	None	0.78	0.19

As shown in Figure 8, there were four primary XPS peaks, 284.8, 532.8, 638.7, and 710.9 eV, belonging to the C1s, O1s, Mn2p, and Fe2p atomic orbitals, respectively. After the Cr(VI) adsorption, the Cr2p peak at 573.6 eV emerged. The results of atom contents showed that the Cr atom content of $MnFe_2O_4$-Cr at pH = 3 was significantly higher than that of $MnFe_2O_4$-Cr at pH = 7 due to the high adsorption quantity of the Cr(VI) under an acidic environment. It is worth noting that the Mn2p atom content declined after Cr(VI) adsorption, implying that the Mn atom in $MnFe_2O_4$ particles was involved in the Cr(VI) reduction reaction. It was inferred that the divalent Mn was oxidized to trivalent Mn by Cr(VI) and entered the solution, resulting in a decrease in the atom content of Mn on the surface of the $MnFe_2O_4$ adsorbent.

To further investigate the adsorption mechanisms of Cr(VI), the high-resolution spectra of Mn2p and Cr2p were conducted. From the Mn2p spectrum of the original $MnFe_2O_4$ adsorbent shown in Figure 9a, there is only one main peak at 641.5 eV of Mn-O considered to belong to the $MnFe_2O_4$. However, after the Cr(VI) adsorption, the peak of MnO_2 emerged, indicating that the Mn(II) on the $MnFe_2O_4$ surface might be oxidized to tetravalence Mn by Cr(VI). In fact, Mn(II) was oxidized to Mn(III) first by Cr(VI). However, the Mn(III) was extremely unstable in an acidic solution and was prone to the disproportionation reaction to form Mn(II) and MnO_2. The resulting Mn(II) could continue to participate in the Cr(VI) reduction, and MnO_2 was deposited on the $MnFe_2O_4$ surface. The XPS results proved that Mn(II) acted as a reductant in the Cr(VI) reduction process.

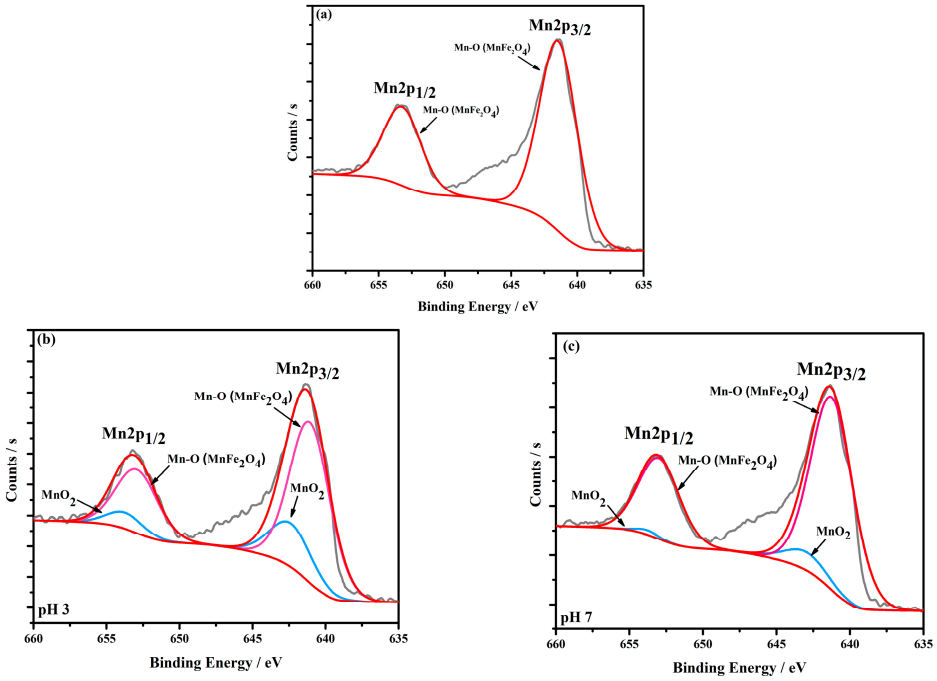

Figure 9. The Mn2p decomposition spectra of $MnFe_2O_4$ (**a**), $MnFe_2O_4$−Cr (pH = 3) (**b**) and $MnFe_2O_4$−Cr (pH = 7) (**c**).

The high-resolution Cr2p spectra of $MnFe_2O_4$-Cr depicted in Figure 10 could be resolved into three individual peaks: The groups of $HCrO_4^-/CrO_4^{2-}$ (577.5 and 587.2 eV), Cr^{3+} (576.2 and 585.9 eV), and $Cr_2O_7^{2-}$ (578.1 and 587.8 eV) [51]. Under the pH = 3 condition, the XPS spectrum showed that the main peak of Cr2p on the $MnFe_2O_4$-Cr surface is Cr(III). When the pH value increased to 7, the dominant species of Cr is Cr(VI). It could be seen that from the XPS results, the Cr adsorbed on the $MnFe_2O_4$ surface, mainly in the form of Cr(III) under pH = 3. This result confirmed that most of the Cr(VI) was reduced to Cr(III) by Mn(II) and formed the $Cr(OH)_3$ compound on the $MnFe_2O_4$ surface. The rest of the Cr adsorbed onto the $MnFe_2O_4$ surface in the form of Cr(VI) via electrostatic adsorption. According to the XPS results, we could speculate that the Cr(VI) was adsorbed on the surface of the $MnFe_2O_4$ adsorbent in the form of chromate. Subsequently, most of the chromate was reduced to Cr(III) by Mn(II).

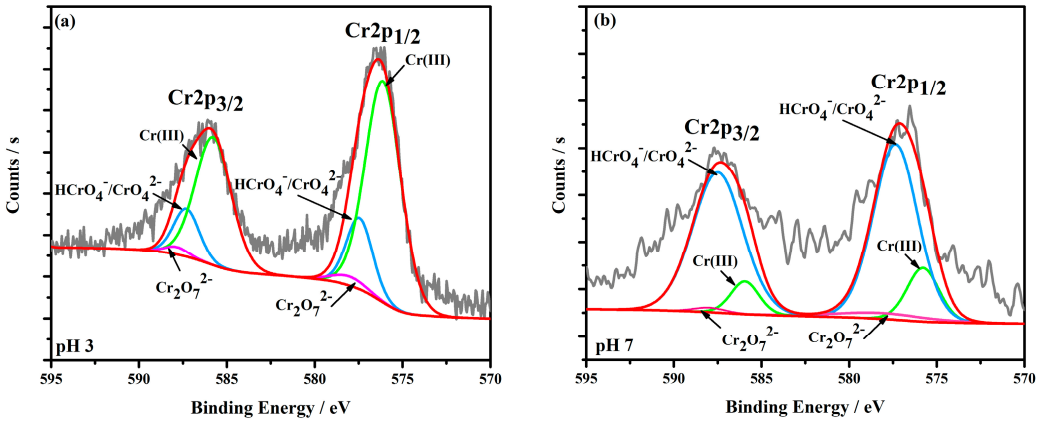

Figure 10. The Cr2p decomposition spectra of $MnFe_2O_4$−Cr at pH = 3 (**a**) and pH = 7 (**b**).

3.4. The Roles of Mn in Cr(VI) Adsorption and Reduction Process

According to the above results, it could be inferred that the roles of Mn in the Cr(VI) removal process could be divided into two parts, providing the adsorbing sites and being a reductant. The Cr(VI) removal process is explained in Figure 11.

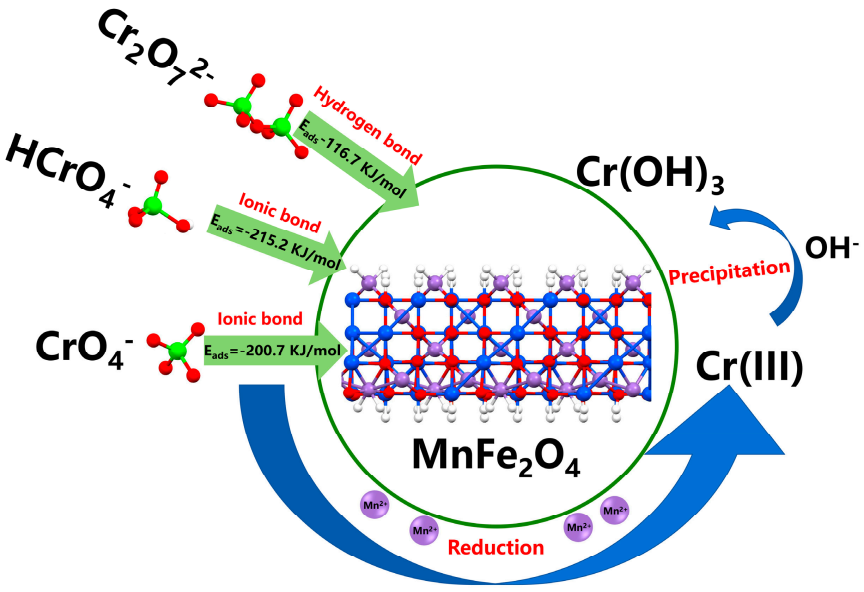

Figure 11. The diagram of the Cr(VI) adsorption and reduction processes.

In the Cr(VI) adsorption process, the Mn atoms of the $MnFe_2O_4$ could form a firm ionic bond with the O atoms of $HCrO_4^-$ and CrO_4^{2-}, thus providing the adsorbing sites for the Cr(VI) adsorption. Then, the adsorbed Cr(VI) was reduced by the Mn(II) dissolved on the $MnFe_2O_4$ surface. In the reduction process, the dissolved Mn(II) acted as a reductant. The Mn(II) first oxidized to Mn(III) by Cr(VI). The unstable Mn(III) would cause the disproportionated reaction and formed Mn(II) and MnO_2 in the aqueous system [52]. The reaction link of the Cr(VI) reduction by Mn(II) can be described by the following equations:

$$3Mn^{2+} + HCrO_4^- + 7H^+ \rightarrow 3Mn^{3+} + Cr^{3+} + 4H_2O \quad (10)$$

$$Cr^{3+} + 3OH^- \rightarrow Cr(OH)_3 \quad (11)$$

$$2Mn^{3+} + 2H_2O \rightarrow Mn^{2+} + MnO_2 + 4H^+ \quad (12)$$

After Cr(VI) reduction, the obtained Cr(III) was complexed with the hydroxy groups to form the inner-sphere complex [53]. The $Cr(OH)_3$ precipitate was deposited on the $MnFe_2O_4$ surface and separated by magnetic separation.

4. Conclusions

The Cr(VI) could be removed efficiently by the $MnFe_2O_4$ adsorbent. The adsorption process belonged to chemisorption. The mechanism research showed that the roles of Mn in the Cr(VI) removal process could be divided into two parts, providing adsorbing sites and being a reductant. The adsorption mechanisms of the Cr(VI) on the $MnFe_2O_4$ adsorbent was the formation of ionic bonds between O atoms of $HCrO_4^-/CrO_4^{2-}$ and the Mn/Fe atoms of the $MnFe_2O_4$ adsorbent, which provided firm adsorbing sites for the Cr(VI). Subsequently, the adsorbed Cr(VI) was reduced by Mn(II) dissolved from the $MnFe_2O_4$ surface. The reduced Cr(III) would form the $Cr(OH)_3$ colloids deposited on the $MnFe_2O_4$ surface, then be removed by magnetic separation. The present work clarified the roles of Mn in the Cr(VI) removal process and provided the removal mechanisms of Cr(VI) on the $MnFe_2O_4$ adsorbent.

Author Contributions: Conceptualization and methodology, Z.S., Y.Z., and Q.L.; methodology, investigation, and writing, M.L.; methodology and supervision, H.Z.; investigation and data curation, J.W.; conceptualization and supervision, T.J. All authors have read and agreed to the published version of the manuscript.

Funding: This research was funded by the National Natural Science Foundation of China, grant numbers 52204276, 52074361, and 51904273.

Data Availability Statement: The data is unavailable due to privacy.

Conflicts of Interest: The authors declare no conflict of interest.

References

1. Mortazavian, S.; Hunyadi Murph, S.E.; Moon, J. Biochar nanocomposite as an inexpensive and highly efficient carbonaceous adsorbent for hexavalent Chromium removal. *Materials* **2022**, *15*, 6055. [CrossRef] [PubMed]
2. Chen, Y.; Zeb, S.; Peng, J.; Zhao, Y.M.; Xu, C.J.; Li, L.; Cui, Y.; Sun, G.X. Enhanced adsorption of Cr(VI) under neutral conditions using a novel adsorbent with preorganized diquaternary ammonium structure. *J. Mol. Liq.* **2021**, *322*, 114905. [CrossRef]
3. Liang, H.X.; Song, B.; Peng, P.; Jiao, G.J.; Yan, X.; She, D. Preparation of there-dimensional honeycomb carbon materials and their adsorption of Cr(VI). *Chem. Eng. J.* **2019**, *367*, 9–16. [CrossRef]
4. Yang, S.Y.; Li, Q.; Chen, L.; Chen, Z.S.; Hu, B.W.; Wang, H.H.; Wang, X.K. Synergistic removal and reduction of U(VI) and Cr(VI) by Fe3S4 micro-crystal. *Chem. Eng. J.* **2020**, *385*, 123909. [CrossRef]
5. Liu, Y.Q.; Shan, H.M.; Zeng, C.Y.; Zhan, H.B.; Pang, Y.Y. Removal of Cr(VI) from Wastewater Using Graphene Oxide Chitosan Microspheres Modified with α–FeO(OH). *Materials* **2022**, *15*, 4909. [CrossRef]
6. Xu, X.Y.; Huang, H.; Zhang, Y.; Xu, Z.B.; Cao, X.D. Biochar as both electron donor and electron shuttle for the reduction transformation of Cr(VI) during its sorption. *Environ. Pollut.* **2019**, *244*, 423–430. [CrossRef] [PubMed]
7. Karthik, C.; Barathi, S.; Pugazhendhi, A.; Ramkumar, V.S.; Thi, N.D.; Arulselvi, P.I. Evaluation of Cr(VI) reduction mechanism and removal by Cellilosimicrobium funkei strain AR8, a novel haloalkaliphilic bacterium. *J. Hazard. Mater.* **2017**, *333*, 42–53. [CrossRef]

8. Han, C.Y.; Yang, L.; Yu, H.L.; Luo, Y.M.; Shan, X. The adsorption behavior and mechanism of Cr(VI) on facile synthesized mesoporous NH-SiO_2. *Environ. Sci. Pollut. R.* **2020**, *27*, 2455–2463. [CrossRef]
9. Arslan, H.; Eskikaya, O.; Bilici, Z.; Dizge, N.; Balakrishnan, D. Comparison of Cr(VI) adsorption and photocatalytic reduction efficiency using leonardite powder. *Chemosphere* **2022**, *300*, 134492. [CrossRef]
10. Zhu, J.L.; Lei, P.; Liu, M.F.; He, P.; Chen, Y.Z.; Gan, M.; Zhu, J.Y. The Interplay of Iron Minerals and Microflora to Accelerate Cr(VI) Reduction. *Materials* **2022**, *12*, 460. [CrossRef]
11. Benettayeb, A.; Ghosh, S.; Usman, M.; Seihoub, F.Z.; Sohoo, I.; Chia, C.H.; Sillanpää, M. Some Well-Known Alginate and Chitosan Modifications Used in Adsorption: A Review. *Water* **2022**, *14*, 1353. [CrossRef]
12. Benettayeb, A.; Morsli, A.; Guibal, E.; Kessas, R. New derivatives of urea-grafted alginate for improving the sorption of mercury ions in aqueous solutions. *Mater. Res. Express* **2021**, *8*, 035303.
13. Vilardi, G.; Palma, L.D.; Verdone, N. A physical-based interpretation of mechanism and kinetics of Cr(VI) reduction in aqueous solution by zero-valent iron nanoparticles. *Chemosphere* **2019**, *220*, 590–599. [CrossRef] [PubMed]
14. Yang, Y.T.; Li, J.; Yan, T.; Zhu, R.X.; Yan, L.G.; Pei, Z.G. Adsorption and photocatalytic reduction of aqueous Cr(VI) by Fe_3O_4-ZnAl-layered double hydroxide/TiO_2 composites. *J. Colloid. Interf. Sci.* **2020**, *562*, 492–504. [CrossRef] [PubMed]
15. Peng, W.J.; Li, H.Q.; Liu, Y.Y.; Song, S.X. A review on heavy metal ions adsorption from water by graphene oxide and its composites. *J. Mol. Liq.* **2017**, *230*, 496–504. [CrossRef]
16. He, F.; Lu, Z.Y.; Song, M.S.; Liu, X.L.; Tang, H.; Huo, P.W.; Fan, W.Q.; Dong, H.J.; Wu, X.Y.; Xing, G.L. Construction of ion imprinted layer modified $ZnFe_2O_4$ for selective Cr(VI) reduction with simultaneous organic pollutants degradation based on different reaction channels. *Appl. Surf. Sci.* **2019**, *483*, 453–462. [CrossRef]
17. Mallik, A.K.; Moktadir, A.M.; Rahman, A.M.; Shahruzzaman, M.; Rahman, M.M. Progress in surface-modified silicas for Cr(VI) adsorption: A review. *J. Hazard. Mater.* **2022**, *423*, 127041. [CrossRef]
18. Lu, M.M.; Zhang, Y.B.; Su, Z.J.; Tu, Y.K.; Wang, J.; Liu, S.; Liu, J.C.; Jiang, T. The comprehensive investigation on removal mechanism of Cr(VI) by humic acid-Fe(II) system structured on V, Ti-bearing magnetite surface. *Adv. Powder. Technol.* **2021**, *32*, 37–51. [CrossRef]
19. Cao, F.M.; Sun, Y.Q.; Zhang, L.; Sun, J. High efficient adsorption accompanied by in-situ reduction of Cr(VI) removal by rice straw fiber ball coated with polypyrrole. *Appl. Surf. Sci.* **2022**, *575*, 151583. [CrossRef]
20. Peng, X.; Liu, S.J.; Luo, Z.J.; Yu, X.W.; Liang, W.W. Selective removal of hexavalent chromium by novel nitrogen and sulfur containing cellulose composite: Role of counter anions. *Materials* **2023**, *16*, 184. [CrossRef]
21. Liang, C.W.; Tang, B.; Zhang, X.D.; Fu, F.L. Mobility and transformation of Cr(VI) on the surface of goethite in the presence of oxalic acid and Mn(II). *Environ. Sci. Pollut. R.* **2020**, *27*, 26115–26124. [CrossRef] [PubMed]
22. Wang, Y.; Chen, S.Y.; Yang, X.; Wu, Y.X.; Huang, X.F.; He, E.K.; Qiu, R.L.; Wang, S.Z. Enhanced removal of Cr(VI) in the Fe(III)/natural polyphenols system: Role of the in situ generated Fe(II). *J. Hazard. Mater.* **2019**, *377*, 321–329. [CrossRef]
23. Mu, Y.; Jiang, Z.; Ai, Z.H.; Jia, F.L.; Zhang, L.Z. Mn^{2+} promoted Cr(VI) reduction with oxalic acid: The indispensable role of In-situ generated Mn^{3+}. *J. Hazard. Mater.* **2018**, *343*, 356–363. [CrossRef]
24. Li, N.; Tian, Y.; Zhao, J.H.; Zhang, J.; Zhang, J.; Zuo, W.; Ding, Y. Efficient removal of chromium from water by Mn_3O_4@ZnO/Mn_3O_4 composite under simulated sunlight irradiation: Synergy of photocatalytic reduction and adsorption. *Appl. Catal. B-Environ.* **2017**, *214*, 126–136. [CrossRef]
25. Islam, M.A.; Angove, M.J.; Morton, D.W.; Pramanik, B.K.; Awual, M.R. A mechanistic approach of chromium (VI) adsorption onto manganese oxides and boehmite. *J. Environ. Chem. Eng.* **2020**, *8*, 103515. [CrossRef]
26. Liu, B.B.; Zhang, Y.B.; Su, Z.J.; Lu, M.M.; Peng, Z.W.; Li, G.H.; Jiang, T. Formation mechanism of $Mn_xFe_{3-x}O_4$ by solid-state reaction of MnO_2 and Fe_2O_3 in air atmosphere: Morphologies and properties evolution. *Powder. Technol.* **2017**, *313*, 201–209. [CrossRef]
27. Eyvazi, B.; Zanjani, A.J.; Darban, A.K. Synthesis of nano-magnetic $MnFe_2O_4$ to remove Cr(III) and Cr(VI) from aqueous solution: A comprehensive study. *Environ. Pollut.* **2019**, *29*, 113685. [CrossRef]
28. He, J.; Lo, I.M.C.; Chen, G.H. Fast removal and recovery of Cr(VI) using surface-modified jacobsite ($MnFe_2O_4$) nanoparticles. *Langmuir* **2005**, *21*, 11173–11179.
29. Ahmadi, A.; Foroutan, R.; Esmaeili, H.; Tamjidi, S. The role of bentonite clay and bentonite clay@$MnFe_2O_4$ composite and their physico-chemical properties on the removal of Cr(III) and Cr(VI) from aqueous media. *Environ. Sci. Pollut. R.* **2020**, *27*, 14044–14057. [CrossRef]
30. Pang, Y.X.; Kong, L.J.; Chen, D.Y.; Yuvaraja, G. Rapid Cr(VI) reduction in aqueous solution using a novel microwave-based treatment with MoS_2-$MnFe_2O_4$ composite. *Appl. Surf. Sci.* **2019**, *471*, 408–416. [CrossRef]
31. Wang, J.; Xu, Q.Y.; Hou, J.H.; Wang, S.S.; Wang, X.Z. Mechanism analysis of $MnFe_2O_4$/FeSX for removal of Cr(VI) from aqueous phase. *Ecotox. Environ. Safe.* **2021**, *217*, 112209. [CrossRef]
32. Tuyen, T.V.; Chi, N.K.; Tien, D.T.; Tu, N.; Quang, N.V.; Huong, P.T.L. Carbon-encapsulated $MnFe_2O_4$ nanoparticles: Effects of carbon on structure, magnetic properties and Cr(VI) removal efficiency. *Appl. Phys. A* **2020**, *126*, 577. [CrossRef]
33. Lin, Y.L.; Chen, J.J.; Cao, W.Z.; Persson, K.M.; Ouyang, T.; Zhang, L.; Xie, X.D.; Liu, F.; Li, J.; Chang, C.T. Novel materials for Cr(VI) adsorption by magnetic titanium nanotubes coated phosphorene. *J. Mol. Liq.* **2019**, *287*, 110826. [CrossRef]

34. Lu, M.M.; Zhang, Y.B.; Zhou, Y.L.; Su, Z.J.; Liu, B.B.; Li, G.H.; Jiang, T. Adsorption-desorption characteristics and mechanisms of Pb(II) on natural vanadium, titanium-bearing magnetite-humic acid magnetic adsorbent. *Powder. Technol.* **2019**, *344*, 947–958. [CrossRef]
35. Liu, S.Y.; Wang, L.J.; Chou, K. Selective chlorinated extraction of iron and manganese from vanadium slag and their application to hydrothermal synthesis of $MnFe_2O_4$. *ACS Sustain. Chem. Eng.* **2017**, *5*, 10588–10596. [CrossRef]
36. Yang, X.; Liu, L.H.; Zhang, M.Z.; Tan, W.F.; Qiu, G.H.; Zheng, L.R. Improved removal capacity of magnetite for Cr(VI) by electrochemical reduction. *J. Hazard. Mater.* **2019**, *374*, 26–34. [CrossRef]
37. Jiang, B.; Gong, Y.F.; Gao, J.N.; Sun, T.; Liu, Y.J.; Oturan, N.; Oturan, M.A. The reduction of Cr(VI) to Cr(III) mediated by environmentally relevant carboxylic acids: State-of-the-art and perspectives. *J. Hazard. Mater.* **2019**, *365*, 205–225. [CrossRef]
38. Guo, X.; Wang, J.L. A general kinetic model for adsorption: Theoretical analysis and modeling. *J. Mol. Liq.* **2019**, *288*, 11100. [CrossRef]
39. Huang, X.P.; Hou, X.J.; Song, F.H.; Zhao, J.C.; Zhang, L.Z. Facet-dependent Cr(VI) adsorption of hematite nanocrystals. *Environ. Sci. Technol.* **2016**, *50*, 1964–1972. [CrossRef]
40. Yazidi, A.; Sellaoui, L.; Dotto, G.L.; Bonilla-Petriciolet, A.; Frohlich, A.C.; Lamine, A.B. Monolayer and multilayer adsorption of pharmaceuticals on activated carbon: Application of advanced statistical physics models. *J. Mol. Liq.* **2019**, *283*, 276–286. [CrossRef]
41. Ma, R.Q.; Wang, T.; Huang, T.B.; Sun, W.L.; Qiao, S.; Liu, W. Insights into the interactions of Cr(III) and organic matters during adsorption onto titanate nanotubes: Differential adsorbance and DFT study. *J. Mol. Liq.* **2020**, *312*, 113432. [CrossRef]
42. Li, M.Q.; Mu, Y.; Shang, H.; Mao, C.L.; Cao, S.Y.; Ai, Z.H.; Zhang, L.Z. Phosphate modification enables high efficiency and electron selectivity of nZVI toward Cr(VI) removal. *Appl. Catal. B-Environ.* **2020**, *263*, 118364. [CrossRef]
43. Robben, B.; Beunis, F.; Neyts, K.; Callens, M.; Johansson, T.; Beales, G.; Fleming, R.; Strubbe, F. Optical evidence for adsorption of charged inverse micelles in a Stern layer. *Colloid. Surface. A* **2020**, *589*, 124451. [CrossRef]
44. Mei, L.J.; Chou, T.H.; Cheng, Y.S.; Huang, M.J.; Yeh, L.H.; Qian, S.Z. Electrophoresis of pH-regulated nanoparticles: Impact of the Stern layer. *Phys. Chem. Chem. Phys.* **2016**, *18*, 9927–9934. [CrossRef]
45. Yin, S.X.; Ellis, D.E. DFT studies of Cr(VI) complex adsorption on hydroxylated hematite (1102) surfaces. *Surf. Sci.* **2009**, *603*, 736–746. [CrossRef]
46. Li, Q.L.; Liu, Y.; Yu, X.F.; Li, L.L.; Zhang, X.H.; Lu, Z.M.; Lin, J.; Yang, X.J.; Huang, Y. Removal of Cr(III)/Cr(VI) from wastewater using defective porous boron nitride: A DFT study. *Inorg. Chem. Front.* **2018**, *5*, 1933–1940. [CrossRef]
47. Zhang, H.L.; Li, P.; Wang, Z.M.; Cui, W.W.; Zhang, Y.; Zhang, Y.; Zheng, S.L.; Zhang, Y. Sustainable disposal of Cr(VI): Adsorption–reduction strategy for treating textile wastewaters with amino-functionalized boehmite hazardous solid wastes. *ACS Sustain. Chem. Eng.* **2018**, *6*, 6811–6819. [CrossRef]
48. Chen, C.S.; Li, H.; Wen, Y.Z.; Zhao, F.; Zhang, Y.P.; Wu, D.L.; Liu, Y.B.; Li, F. Spherical Cu_2O-Fe_3O_4@chitosan bifunctional catalyst for coupled Cr-organic complex oxidation and Cr(VI) capture-reduction. *Chem. Eng. J.* **2020**, *383*, 123105.
49. Bader, R.F.W.; Henneker, W.H. The ionic bond. *J. Am. Chem. Soc.* **1965**, *87*, 3063–3068. [CrossRef]
50. Howard, S.T.; Lamarche, O. Description of covalent bond orders using the charge density topology. *J. Org. Chem.* **2003**, *16*, 133–141. [CrossRef]
51. Park, D.; Yun, Y.S.; Park, J.M. XAS and XPS studies on chromium-binding groups of biomaterial during Cr(VI) biosorption. *J. Colloid. Interf. Sci.* **2008**, *317*, 54–61. [CrossRef] [PubMed]
52. Qian, A.; Zhang, W.; Shi, C.; Pan, C.; Giammar, D.E.; Yuan, S.; Zhang, H.L.; Wang, Z.M. Geochemical Stability of Dissolved Mn(III) in the Presence of Pyrophosphate as a Model Ligand: Complexation and Disproportionation. *Environ. Sci. Technol.* **2019**, *53*, 5768–5777. [CrossRef] [PubMed]
53. Xie, J.Y.; Gu, X.Y.; Tong, F.; Zhao, Y.P.; Tan, Y.Y. Surface complexation modeling of Cr(VI) adsorption at the goethite–water interface. *J. Colloid. Interf. Sci.* **2015**, *455*, 55–62. [CrossRef] [PubMed]